

## Research Article

Zhongkun Niu, Zhengming Yang, Yutian Luo, Yapu Zhang, Xinli Zhao\*, Yilin Chang, and Xinliang Chen\*

# Study on fine characterization and reconstruction modeling of porous media based on spatially-resolved nuclear magnetic resonance technology

<https://doi.org/10.1515/phys-2022-0204>

received September 26, 2021; accepted October 07, 2022

**Abstract:** At present, image analysis and digital core are the main approaches for porous media reconstruction modeling, and they are both based on the real pore skeleton physical structure of porous media. However, it is difficult to reconstruct the reservoir and seepage characteristics of the real samples because of the limitations of accuracy in characterization techniques (imaging). In order to solve this problem and break through the barriers caused by the lack of accuracy, Spin-echo serial peripheral interface sequence of low field nuclear magnetic resonance is used to test the saturated water rock core with spatially resolved  $T_2$  distributions. Based on the experimental results of 1D  $T_2$  distributions, a novel method for fine reconstruction modeling of porous media is proposed, and the porous media model reconstructed by this new method better reproduces the reservoir and

seepage characteristics of the original samples. Taking some of the tested porous media cores (P58 and Y75) as examples, representative elementary volume (REV)-lattice Boltzmann method (LBM) is used to simulate the flow field. Ensuring that the error of standard case is only 0.36% when multi-relaxation time REV-LBM is used, the distribution of porosity and permeability have been calculated and compared with the experimental data. The overall permeability error of the reconstructed porous media model is only 6.15 and 7.60%, respectively. Furthermore, the porosity and permeability error of almost all measuring points can be maintained within 3 and 8%. In addition, this method improves the efficiency of the existing reconstruction modeling methods, reduces the test cost, and makes the reconstruction modeling of porous media easier to operate, which has promising development prospects.

**Keywords:** spatially resolved  $T_2$  distributions, reconstruction model, porous media, nuclear magnetic resonance, REV-LBM

\* **Corresponding author: Xinli Zhao**, School of Petroleum Engineering, Changzhou University, Changzhou, 213164, China, e-mail: [ucaszxl@163.com](mailto:ucaszxl@163.com)

\* **Corresponding author: Xinliang Chen**, University of Chinese Academy of Sciences, Beijing, 100049, P. R. China; Institute of Porous Flow and Fluid Mechanics, Chinese Academy of Sciences, Langfang, Hebei 065007, China; Department of Porous Flow & Fluid Mechanics, Research Institute of Petroleum Exploration & Development, PetroChina Company Limited, Langfang, Hebei 065007, China, e-mail: [chenxinliang20@mails.ucas.edu.cn](mailto:chenxinliang20@mails.ucas.edu.cn)

**Zhongkun Niu, Yutian Luo, Yilin Chang:** University of Chinese Academy of Sciences, Beijing, 100049, P. R. China; Institute of Porous Flow and Fluid Mechanics, Chinese Academy of Sciences, Langfang, Hebei 065007, China; Department of Porous Flow & Fluid Mechanics, Research Institute of Petroleum Exploration & Development, PetroChina Company Limited, Langfang, Hebei 065007, China

**Zhengming Yang, Yapu Zhang:** Institute of Porous Flow and Fluid Mechanics, Chinese Academy of Sciences, Langfang, Hebei 065007, China; Department of Porous Flow & Fluid Mechanics, Research Institute of Petroleum Exploration & Development, PetroChina Company Limited, Langfang, Hebei 065007, China

## 1 Introduction

Accurate characterization of porous media is the key to study porous media seepage mechanism. At present, the main research methods mainly include experimental testing technology, image analysis, and digital core analysis. The main methods of experimental testing are rate-controlled mercury intrusion [1], high-pressure mercury intrusion [2,3], low-temperature nitrogen adsorption [4], and nuclear magnetic resonance (NMR) [5,6]. Image analysis technology mainly relies on the images obtained through thin section [7] or scanning electron microscope [8] for further analysis. Digital core technology is digital reconstruction of porous media, which mainly relies on digital image processing technology combined with X-ray micro computed tomography (Micro-CT) [9].

At present, image analysis technology and digital core analysis are the main methods to reconstruct the porous media model. Among them, image analysis technology is able to reconstruct the 2D porous media model by identifying the mineral component boundary or by using the statistical parameters of porous media obtained from the image to generate random porous media by random process [10], while digital core technology reconstructs 3D model by processing multi-layer micro-CT scan images [11,12]. Although there are some differences between them, the idea of reconstructing the model according to the real pore skeleton physical structure of porous media is the same. That is why the reconstructed porous media model cannot better reproduce the reservoir or seepage characteristics of the original real samples because of the limitation of present machine scanning accuracy. Therefore, there is an urgent need for a method to reconstruct the porous media, which can break through this hardware defect, and the reconstructed porous media model can better reproduce the reservoir and seepage characteristics of the original real samples.

Referring to the description of porous media model in lattice Boltzmann method (LBM) [13,14], the concept model of porous media can be divided into two categories. One is to finely describe pore throat structure and micro-cracks, distinguish pores and skeletons, and treat porous media as discrete media, as pore-scale model. The other, as representative elementary volume (REV)-scale model, is to avoid the fine description of pore throat structure, and describe the porous media as lots of smaller scale porous media, each local area has local porosity and local permeability. Among them, the first type is concept model for the current image analysis technology or digital core technology [15], while the second type of conceptual model is the key to break through the above hardware limitations and solve the problem.

NMR can quickly and efficiently capture the reservoir and seepage characteristics of porous media. The Carr–Purcell–Meiboom–Gill (CPMG) sequence can be used to measure the transverse relaxation time ( $T_2$ ) [16]. While the Spin-Echo Serial Peripheral Interface (SE-SPI) sequence divides the core into multiple layers, and obtains the  $T_2$  distribution spectrum of each layer by coding [17,18], it is not as accurate as CPMG sequence. But SE-SPI is sensitive to the signal of mobile fluids in porous media [19]. Therefore, based on the spatially resolved  $T_2$  distribution measurement of SE-SPI sequence, combined with the macro parameters of porous media and Fractal Brownian motion, this study uses Gauss stochastic process to generate the porous media reconstruction model. Compared with image analysis technology or digital core technology, the new reconstruction

method of porous media model proposed in this study solves the problem that the reconstruction model is difficult to reproduce the real sample reservoir and seepage characteristics due to hardware constraints. At the same time, the new reconstruction method of porous media model also has the advantages of short test cycle, simple sample processing, and low experimental cost.

## 2 Materials and experiment

### 2.1 Materials and instruments

Low-permeability tight sandstone core, formation water with certain salinity, raw tape, silicone oil calibration bottle, high-temperature drying oven, vacuum pump, core holder, intermediate container, and NMR instrument were used in this experiment.

### 2.2 Experimental method

The flow chart of the experiment is shown in Figure 1, while more detailed experimental steps are as follows.

- 1) Determination of basic physical parameters: select eleven tight sandstone cores and then determine the basic physical parameters such as dry gas permeability and porosity. The specific physical parameters are shown in Table 1.

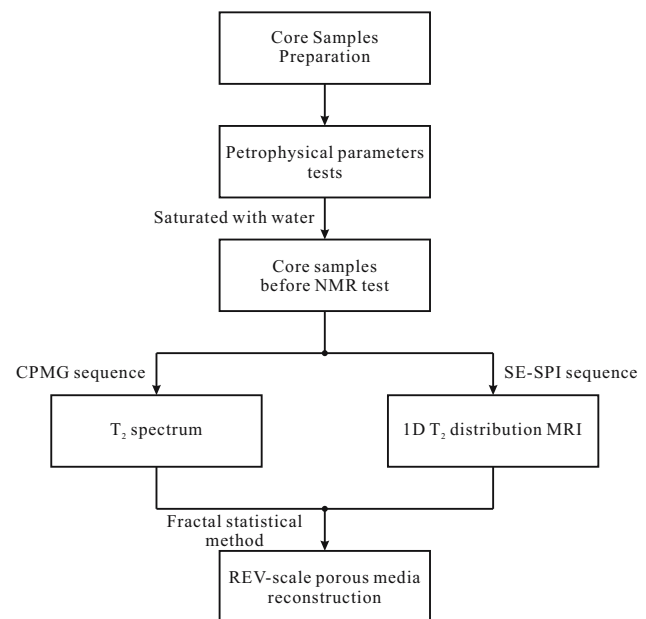


Figure 1: Flowchart of the designed experiment.

**Table 1:** Porous media parameters of the tight sandstone samples

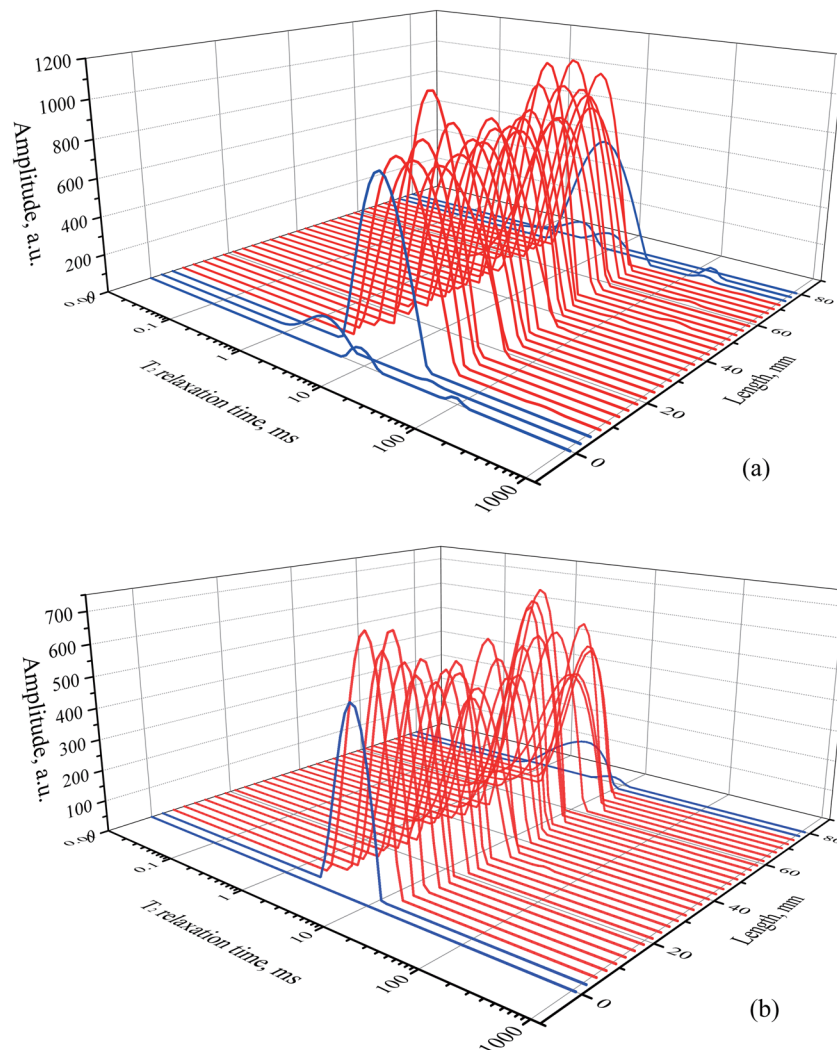
Samples	Length (cm)	Volume (cm <sup>3</sup> )	Porosity (%)	Permeability (10 <sup>-3</sup> μm <sup>2</sup> )
Y75	7.043	37.051	9.662	0.03804
Y76	7.370	34.183	9.787	0.02949
Y95	6.890	34.917	10.33	0.04810
Y100	7.354	36.941	9.599	0.03686
P58	6.744	35.323	16.11	4.655
P60	6.906	34.583	17.05	3.531
R37	6.929	34.773	8.830	0.5346
R38	6.778	33.957	8.931	0.5404
P24	6.521	33.921	10.16	1.418
P28	6.703	34.193	13.60	2.893
P41	6.678	33.997	5.891	1.514

- 2) Saturated core: put the first 8 cores into the high-temperature drying oven for drying for 8 h, put it into the pressure vessel for vacuumizing for 1 day, and select

the compatible formation water for pressure saturation for 1 day.

- 3) Sample loading: after calibrating NMR parameters with silicone oil bottle, the core is wrapped with tape and put into NMR instrument to ensure that the core is in the middle of the observation window (8 cm).
- 4) Determination of overall  $T_2$  distribution: the whole transverse NMR  $T_2$  relaxation spectra of each core are determined by Q-CPMG sequence (SF = 12 MHz, O1 = 496668.7 Hz, P1 = 21 μs, and P2 = 40.48 μs).
- 5) Determination of stratified  $T_2$  distribution: SE-SPI sequence (SF = 12 MHz, O1 = 496668.7 Hz, P1 = 21 μs, and P2 = 40.48 μs) is used to determine the transverse NMR  $T_2$  relaxation spectra of each core layer according to the number of setting layers of 31, that is, 1D  $T_2$  distribution magnetic resonance imaging (MRI).

Because the length of the observation window is larger than that of the core, when the interval between

**Figure 2:** 1D  $T_2$  distribution MRI of P58 sample (a) and Y75 sample (b) (blue curves need to be omitted, while red curves have to be reserved).

layers is lower than a certain value, there is  $T_2$  distribution spectrum at both ends of the tested 1D  $T_2$  distribution MRI whose signal quantity is approximately 0. Take core P58 and Y75 as example, the  $T_2$  distribution spectrum of each layer measured by spatially resolved NMR is shown in Figure 2. In order to ensure that the  $T_2$  distribution spectrum of each layer used in the subsequent reconstruction of porous media has the same length, we remove the test curve with large signal difference at both ends.

### 3 REV-scale porous media reconstruction

REV-scale porous media reconstruction is also a method for fine characterization of porous media from the perspective of porous media parameters, distinguished with the digital core method which considers the structure of pore-throat network. The difference is that digital core is based on the physical structure of pore skeleton porous media, the porous media model constructed by digital core belongs to 0–1 coverage model, while REV-scale porous media reconstruction is from the perspective of fluid seepage, and the porous media model (Figure 3) belongs to gray model with the distribution maps of local porosity and local permeability.

The new method of porous media reconstruction is based on spatially resolved nuclear magnetic technology,

through which the actual core porosity or permeability and other physical parameters cannot be obtained directly, it is necessary to use some  $T_2$  distribution spectrum eigenvalues to obtain the corresponding physical parameters. Among them, the peak area of signal per unit volume can be used to describe the porosity of porous media, while the eigenvalues related to  $T_2$  geometric mean ( $T_{2gm}$ ) and porosity calculated by Schlumberger Doll Research (SDR) model [20,21] can characterize the permeability of porous media. Combined with the porosity, permeability, and the corresponding characteristic values obtained from the overall  $T_2$  distribution spectrum of eleven cores, it is found that the signal peak area per unit volume is approximately proportional to porosity (Figure 4), while the characteristic value of SDR model is approximately proportional to permeability (Figure 5).

Considering that rock is a kind of material with self-similar fractal characteristics, this study reconstructs REV-scale porous media from the perspective of effective porosity and seepage capacity of porous media based on the abovementioned concept of reconstructing porous media model and  $T_2$  distribution spectrum model theory and fractal topology theory. The specific algorithm flow is shown in Figure 6.

#### 3.1 Fractal parameters acquisition

The signal peak area per unit volume is noted as  $A$ , which meets the requirement  $\bar{A} = \frac{1}{n} \sum_i^n A_i$ . And the distribution of

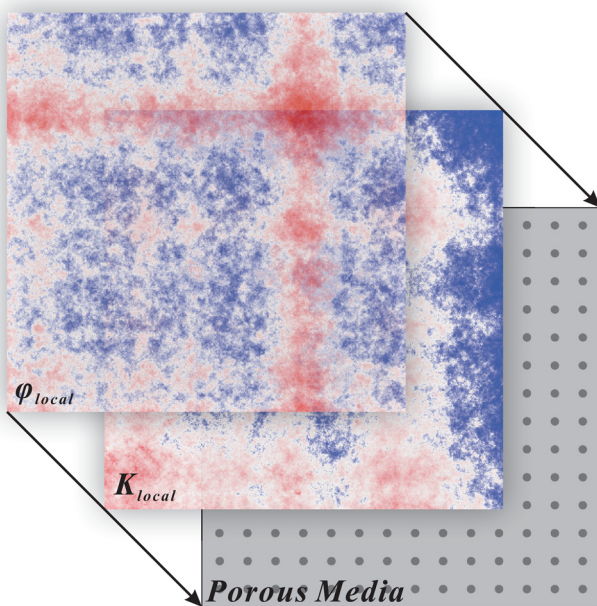


Figure 3: Conceptual graph of porous media's reconstruction model.

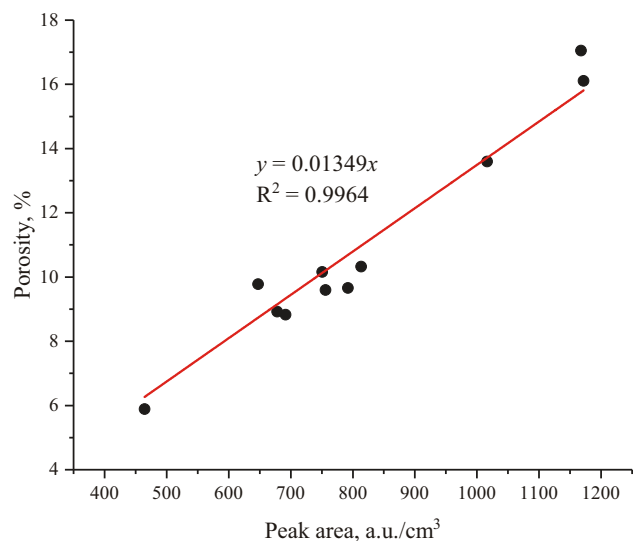


Figure 4: The scatter diagram between porosity and signal peak area (the red curve denotes the linear fitting curve).



$A$  is proportional to porosity  $\varphi$ , the distribution is supposed to be similar, with statistical regularity. Considering that the relationship between the overall geometric mean value of  $T_2$  and each layer can be expressed as  $\bar{T}_{2gm} = \prod_i^n T_{2gm,i}^{\varphi_i/n\varphi} = \prod_i^n T_{2gm,i}^{A_i/n\bar{A}}$  in the SDR model, after taking logarithm, it becomes  $\bar{A} \ln \bar{T}_{2gm} = \frac{1}{n} \sum_i^n (A_i \ln T_{2gm,i})$ . Taking  $A \ln T_{2gm}$  as  $T_{2A}$ , which is similar to  $A$  and can be used to reflect the movable fluid with statistical regularity, then  $\bar{T}_{2A} = \frac{1}{n} \sum_i^n T_{2A,i}$ .

In order to describe the random signal with statistical characteristics,  $B(x)$  is defined as a 1D scattered point sequence conforming to the fractal Brownian motion to describe the characteristics of Fractal Brownian motion by Hurst exponent ( $H$ ) and  $\sigma_0$  standard deviation under reference distance  $\Delta_0$  ( $\sigma_0$ ). According to the definition of Fractal Brownian motion, two methods can be derived [22,23], including direct method and indirect method, to obtain the  $H$  and  $\sigma_0$  of  $A$  and  $T_{2A}$ .

1) The direct method. According to its definition,

$D[B(x + \Delta) - B(x)] \sim |\Delta/\Delta_0|^{2H}$  can be derived as follows:

$$\frac{1}{2} \ln \{D[B(x + \Delta) - B(x)]\} = H \ln(\Delta/\Delta_0) + \ln \sigma_0, \quad (1)$$

where  $D(x)$  is the mean square deviation of the dataset  $x$ .

Based on the experiment data of Y75, draw the scatter diagram of  $\frac{1}{2} \ln \{D[B(x + \Delta) - B(x)]\}$  vs  $\ln(\Delta/\Delta_0)$  (Figure 7), and fit the straight-line segment, where the slope is  $H$  and the intercept is  $\ln \sigma_0$ .

2) The indirect method. From the definition  $[B(x + \Delta) - B(x)] \sim$

$N(0, \sigma^2)$  and  $E[|B(x + \Delta) - B(x)|] = \sqrt{\frac{2}{\pi}} \sigma$  can be calcu-

lated, and the equation  $E[|B(x + \Delta) - B(x)|] \sim |\Delta/\Delta_0|^H$  is able to be obtained from the definition. So, the following equation can be derived.

$$\begin{aligned} & \ln \{E[|B(x + \Delta) - B(x)|]\} \\ &= H \ln(\Delta/\Delta_0) + \left[ \ln \sigma_0 + \frac{1}{2} (\ln 2 - \ln \pi) \right], \end{aligned} \quad (2)$$

where  $E(x)$  is the mean (mathematical expectation) of the dataset  $x$ .

Based on the experiment data of Y75, draw the scatter diagram of  $\ln \{E[|B(x + \Delta) - B(x)|]\}$  vs  $\ln(\Delta/\Delta_0)$  (Figure 8), and fit the straight-line segment, where the slope is  $H$  and the intercept is  $\ln \sigma_0 + \frac{1}{2} (\ln 2 - \ln \pi)$ .

The Hurst exponent of two parameters  $A$  and  $T_{2A}$  of each core can be calculated by using the above two algorithms, as shown in Table 2.

Drawing the scatter diagram of  $R$ -squared vs Hurst exponent, which is shown in Figure 9, and the difference between the results obtained from two methods can be observed. When  $R$ -squared  $> 0.9$ ,  $H_A$  from direct method is in the range of 0.188–0.479, and  $H_{T_{2A}}$  is in the range of

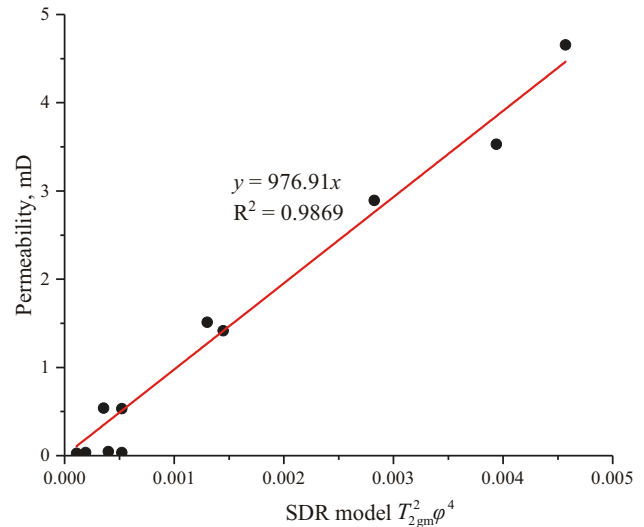


**Figure 5:** The scatter diagram between permeability and SDR model (the red curve denotes the linear fitting curve).

0.243–0.447. It is found that the distribution ranges of these two Hurst exponents roughly coincide. However, the situation is different for indirect method. When  $R$ -squared  $> 0.9$ , the distribution of  $H'_A$  is in the range of 0.145–0.406, but  $H'_{T_{2A}}$  is in the range of 0.343–0.595. The distribution ranges of  $H'_A$  and  $H'_{T_{2A}}$  are distinguished. It is obvious that the two methods have differences in calculation results, and further analysis is needed to screen the methods.

### 3.2 2D fractal seed determination

Since the test data obtained by spatially resolved NMR is 1D  $T_2$  distribution MRI, the reconstructed model based on  $B(x)$  must be 1D model. If the model of the corresponding dimension is expected, the fractal seed of the corresponding dimension is necessary. Take the 2D model as an example, the 2D fractal seed is needed. Considering that the outer product of two sets of sequences conforming to the fractal Brownian motion can produce a 2D fractal seed (Appendix I) which also satisfies the fractal Brownian motion, that is,  $B_{2D}(x, y) = \alpha |B(x)\rangle \langle B(y)|$ , where  $\alpha$  is the coefficient. For the same porous medium, the mean value characterizes it from a macro-perspective, the change in dimension will not change the mean value, which is expressed as  $E[B_{2D}(x, y)] = E[B(x)] = E[B(y)] = \mu_B$ , where  $\alpha = \frac{1}{\mu_B}$  and the 2D fractal seed is described as follows:

$$B_{2D}(x, y) = \frac{|B(x)\rangle \langle B(y)|}{\mu_B}. \quad (3)$$

After the 2D fractal seed is determined, the corresponding fractal parameters, i.e.,  $H$  and  $\sigma_0$ , need to be

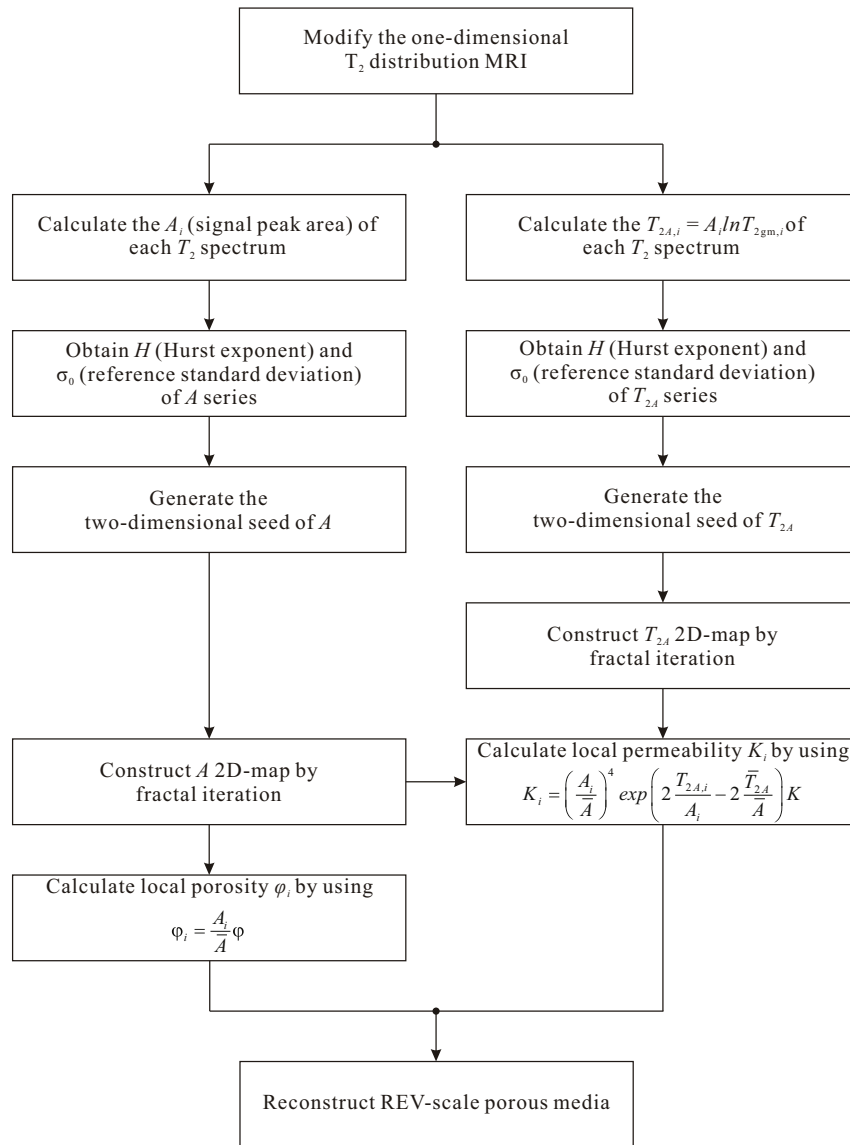


Figure 6: Flowchart of porous media model reconstruction algorithm.

calculated. Because the 2D fractal seed involves two directions, it has four fractal characteristic parameters,  $H_x$ ,  $H_y$ ,  $\sigma_{0x}$ , and  $\sigma_{0y}$ . Under this situation, only indirect method can guarantee the consistent invariance of Hurst exponent calculated under different dimensions, while the Hurst exponent calculated by direct method will change with the change in dimension (Appendix II). Therefore, in order to ensure the consistency of the fractal characteristic parameters calculated under different dimensions, the indirect method should be selected to calculate the fractal characteristic parameters.

### 3.3 1D fractal interpolation method

Define  $r$  as shrink factor. For the fractal value (Figure 10) before and after scaling  $r$  times, it can be simply expressed as linear model plus random number, where the random number  $Rn$  conforms to normal distribution, i.e.,  $Rn \sim N(\mu, \sigma^2)$ .

$$B(x + r\Delta_0) - B(x) = r[B(x + \Delta_0) - B(x)] + Rn. \quad (4)$$

For Eq. (4), the expectation and variance are obtained, respectively

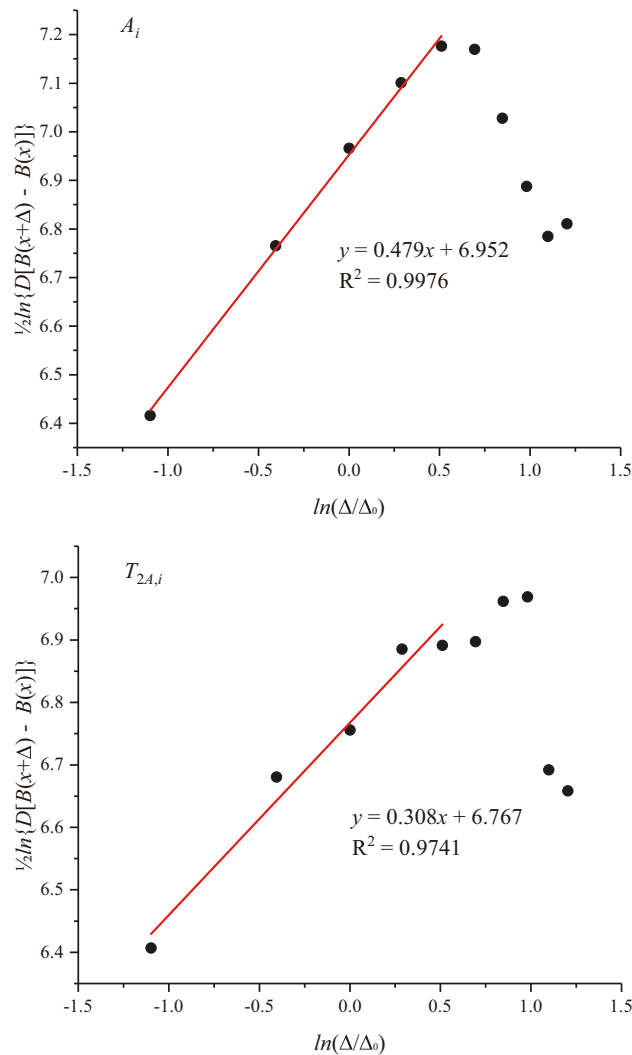


**Figure 7:** The scatter diagram obtained by direct method (the red curve is the linear segment fitting straight line).

$$E[B(x + r\Delta_0) - B(x)] = rE[B(x + \Delta_0) - B(x)] + E(Rn), \quad (5)$$

$$D[B(x + r\Delta_0) - B(x)] = r^2D[B(x + \Delta_0) - B(x)] + D(Rn). \quad (6)$$

Note  $E[B(x + \Delta_0) - B(x)] = \mu_0$  and  $D[B(x + \Delta_0) - B(x)] = \sigma_0^2$ . Combined with the properties of Fractal Brownian motion, we can get the following conclusions:  $E[B(x + r\Delta_0) - B(x)] = \mu_0 = 0$  and  $D[B(x + r\Delta_0) - B(x)] = r^{2H}\sigma_0^2$ . The expectation and variance of the random number  $Rn$  can be obtained,  $E(Rn) = 0$  and  $D(Rn) = (r^{2H} - r^2)\sigma_0^2 = r^{2H}(1 - r^{2-2H})\sigma_0^2$ .

After processing,

$$B(x + r\Delta_0) = rB(x + \Delta_0) + (1 - r)B(x) + Rn, \quad (7)$$

$$Rn \sim N(\mu, \sigma^2),$$

where,  $\mu = 0$  and  $\sigma = r^H\sqrt{1 - r^{2-2H}}\sigma_0$ .

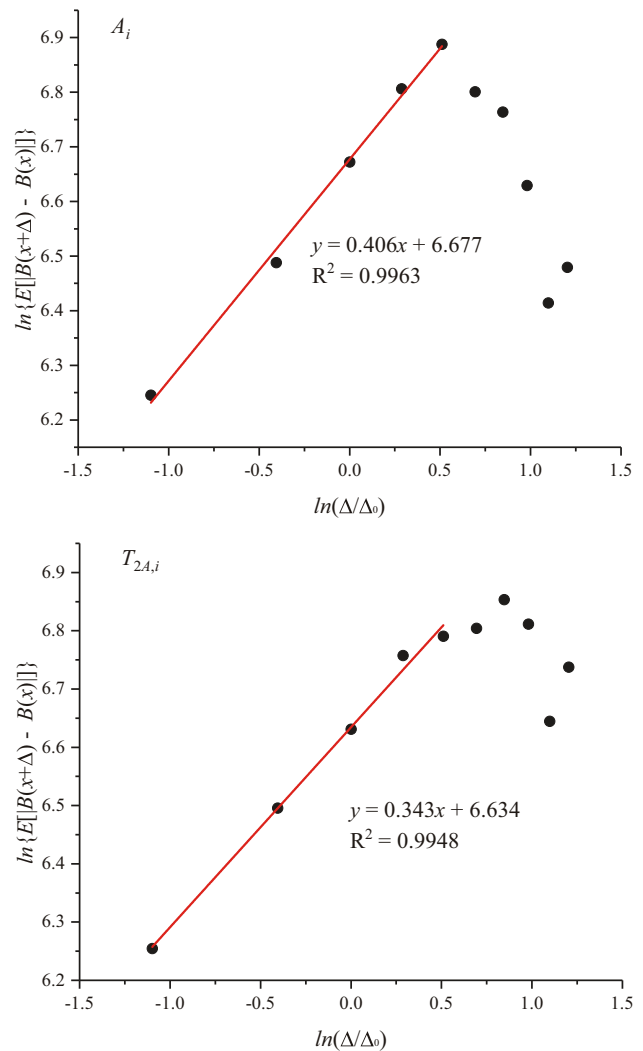


**Figure 8:** The scatter diagram obtained by indirect method (the red curve is the linear segment fitting straight line).

In particular, Eq. (7) is degenerated to the formula of random midpoint displacement [24], that is,

$$B\left(x + \frac{1}{2}\Delta_0\right) = \frac{1}{2}[B(x + \Delta_0) + B(x)] + Rn, \quad (8)$$

$$Rn \sim N(\mu, \sigma^2),$$

where  $\mu = 0$  and  $\sigma = 2^{-H}\sqrt{1 - 2^{2H-2}}\sigma_0$ .

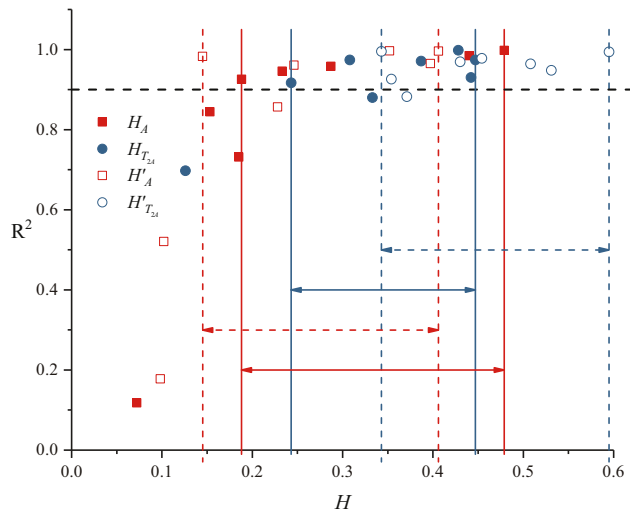
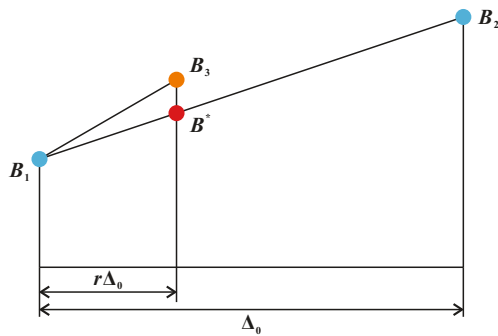
### 3.4 2D fractal interpolation method

By analogy with the fractal interpolation algorithm in 1D, square<sub>0</sub> is scaled to square<sub>1</sub>, the scaling factor is  $\frac{\sqrt{2}}{2}$ , as shown in Figure 11. The interpolation point  $B_5$  is located

**Table 2:** Hurst exponent form of samples calculated by two different methods

Samples	$H_A$	$H'_A$	$H_{T2A}$	$H'_{T2A}$
Y75	0.479 (0.998 <sup>+</sup> )	0.406 (0.996)	0.308 (0.974)	0.343 (0.995)
Y76	0.153 (0.845)	0.145 (0.983)	0.428 (0.998)	0.430 (0.969)
Y95	0.188 (0.926)	0.246 (0.961)	0.387 (0.971)	0.531 (0.948)
Y100	0.233 (0.946)	0.228 (0.857)	0.447 (0.974)	0.595 (0.994)
P58	0.440 (0.985)	0.397 (0.965)	0.333 (0.880)	0.371 (0.882)
P60	0.287 (0.958)	0.352 (0.997)	0.442 (0.930)	0.508 (0.964)
R37	0.072 (0.118)	0.098 (0.178)	0.126 (0.698)	0.454 (0.978)
R38	0.185 (0.732)	0.102 (0.521)	0.243 (0.917)	0.354 (0.926)

(\*Number in brackets is  $R$ -squared,  $H_A$  and  $H_{T2A}$  are calculated by direct method,  $H'_A$  and  $H'_{T2A}$  are calculated by indirect method.).

**Figure 9:** Different Hurst exponent distribution map.**Figure 10:** Schematic diagram of 1D fractal interpolation ( $B^*$  is linear interpolation point, while  $B_3$  is fractal interpolation point).

in the center of square<sub>0</sub>. Compared with the four vertices  $B_1$ ,  $B_2$ ,  $B_3$ , and  $B_4$ , four 1D fractal interpolation expressions can be constructed.

$$B_5 - B_1 = \frac{\sqrt{2}}{2}(B_2 - B_1) + Rn_1, \quad (9)$$

$$B_5 - B_2 = \frac{\sqrt{2}}{2}(B_3 - B_2) + Rn_2, \quad (10)$$

$$B_5 - B_3 = \frac{\sqrt{2}}{2}(B_4 - B_3) + Rn_3, \quad (11)$$

$$B_5 - B_4 = \frac{\sqrt{2}}{2}(B_1 - B_4) + Rn_4, \quad (12)$$

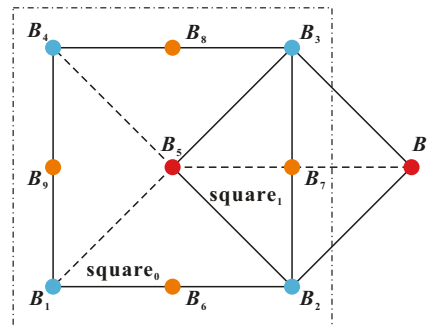
The random numbers,  $Rn_1$ ,  $Rn_2$ ,  $Rn_3$ , and  $Rn_4$  all conform to the normal distribution, and can be obtained by adding Eqs. (9)–(12),

$$B_5 = \frac{1}{4}(B_1 + B_2 + B_3 + B_4) + \frac{1}{4}(Rn_1 + Rn_2 + Rn_3 + Rn_4). \quad (13)$$

Considering that  $B_5$  is unique, therefore,  $Rn_1$ ,  $Rn_2$ ,  $Rn_3$ , and  $Rn_4$  are completely related, and there is only one random variable, Eq. (3) can be simplified as

$$B_5 = \frac{1}{4}(B_1 + B_2 + B_3 + B_4) + Rn, \quad Rn \sim N(\mu, \sigma^2). \quad (14)$$

The random numbers  $Rn$ ,  $Rn_1$ ,  $Rn_2$ ,  $Rn_3$ , and  $Rn_4$  satisfy the same normal distribution, that is  $\mu = 0$  and  $\sigma = 2^{-H/2}\sqrt{1 - 2^{H-1}}\sigma_0$ .

**Figure 11:** Schematic diagram of 2D fractal interpolation ( $B^*$  is the center point of another square<sub>0</sub> that may not exist).



For interpolation points  $B_6$ ,  $B_7$ ,  $B_8$ , and  $B_9$ , although they can be regarded as the center points of square<sub>1</sub> after one iteration, Eq. (14) can be used for calculation. However, to avoid the situation of the lack of numerical value of  $B^*$  and improve the parallel ability of calculation,  $B_6$ ,  $B_7$ ,  $B_8$ , and  $B_9$  are only treated as 1D interpolation points.

### 3.5 Conversion of fractal values to porous media parameters

Using the fractal algorithm in the previous section, a map of certain size about  $A$  or  $T_{2A}$  can be iteratively generated. Because of the conclusion in the Section 1, the peak area of unit volume signal is approximately proportional to

the local porosity, and the eigenvalue of SDR model is approximately proportional to the local permeability, two basic expressions can be obtained

$$\frac{\varphi_i}{\varphi} = \frac{A_i}{\bar{A}}, \quad (15)$$

$$\frac{K_i}{K} = \frac{T_{2gm,i}^2 \varphi_i^4}{\bar{T}_{2gm}^2 \varphi^4}. \quad (16)$$

Considering the definitions of  $A$  and  $T_{2A}$  (Section 3.1), Eqs. (15) and (16) can be sorted into

$$\varphi_i = \frac{A_i}{\bar{A}} \varphi, \quad (17)$$

$$K_i = \left(\frac{A_i}{\bar{A}}\right)^4 \exp\left(2\frac{T_{2A,i}}{A_i} - 2\frac{\bar{T}_{2A}}{\bar{A}}\right) K. \quad (18)$$

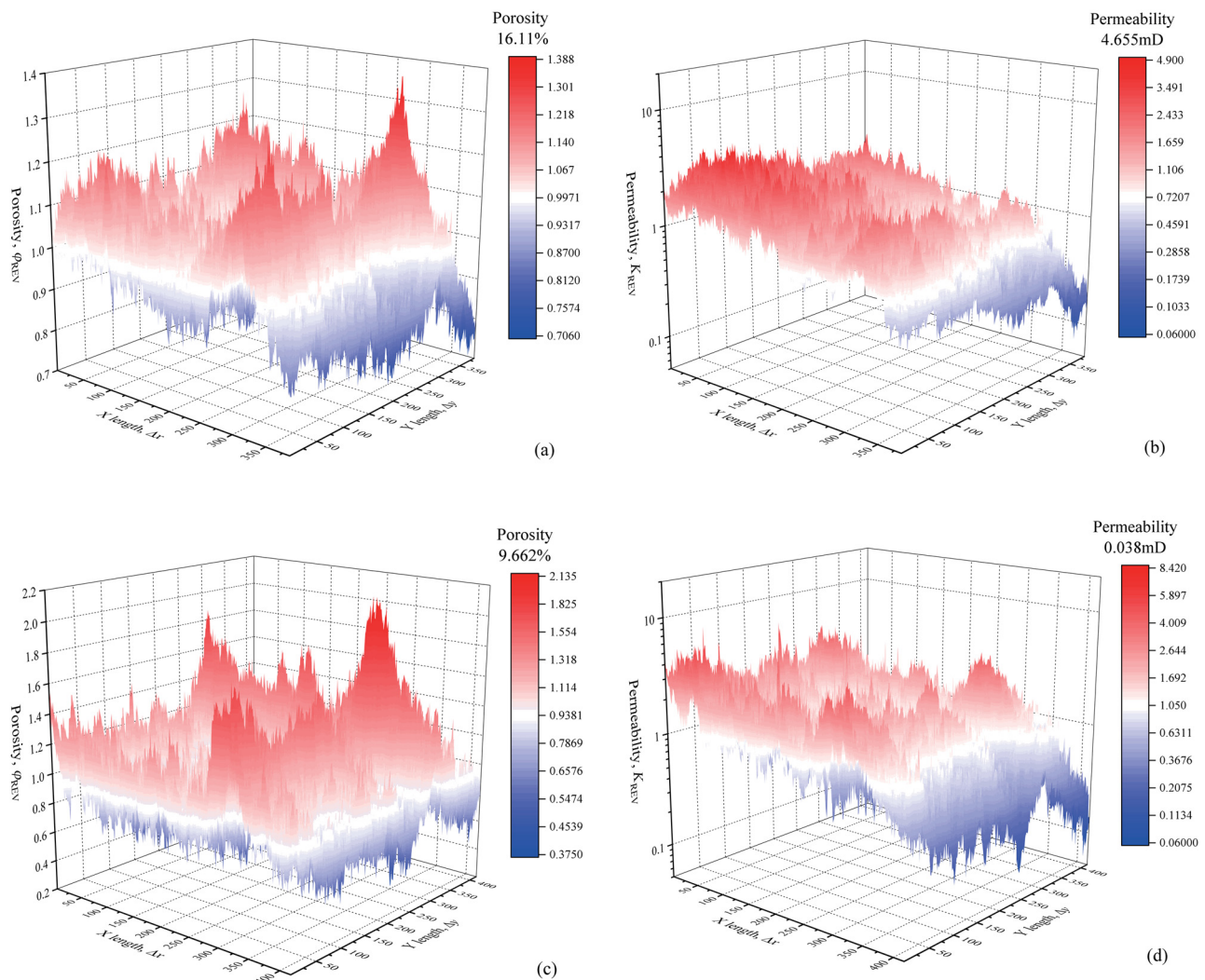


**Figure 12:** Porosity distribution 3D-color map of P58 samples (a) and Y75 samples (c) reconstruction model, and permeability distribution 3D-color map of P58 samples (b) and Y75 samples (d) reconstruction model.

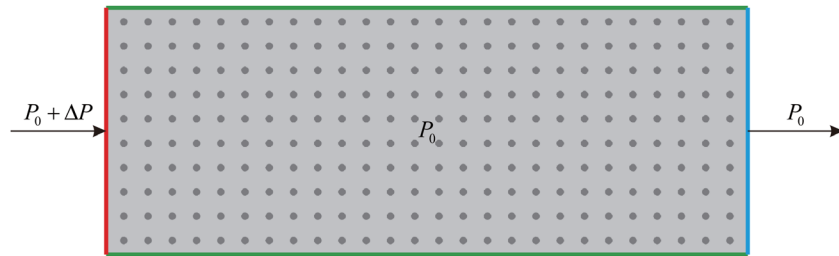


Figure 13: Physical model (Red: pressure boundary; Blue: free boundary; Green: periodic boundary).

## 4 The algorithm of porous media reconstruction application testing

### 4.1 Reconstruction of porous media model

In the following application testing, P58 and Y75 were selected as demonstration cases. Here  $B(y) = B(x)$  (the

same fractal characteristics in the length and width direction) was assumed because only 1D  $T_2$  distribution MRI in length direction had been obtained from the experiment. In addition, this simple assumption  $B(y) \neq \mu_B$  can prove whether the fractal features in 1D will be affected by the change in dimension. Referring to Eq. (3), the 2D fractal seed could be calculated easily. Then, the seed can be expanded to a 2D map of certain length and width about  $A$  or  $T_{2A}$  with the usage of Eq. (8) and (14), and the fractal

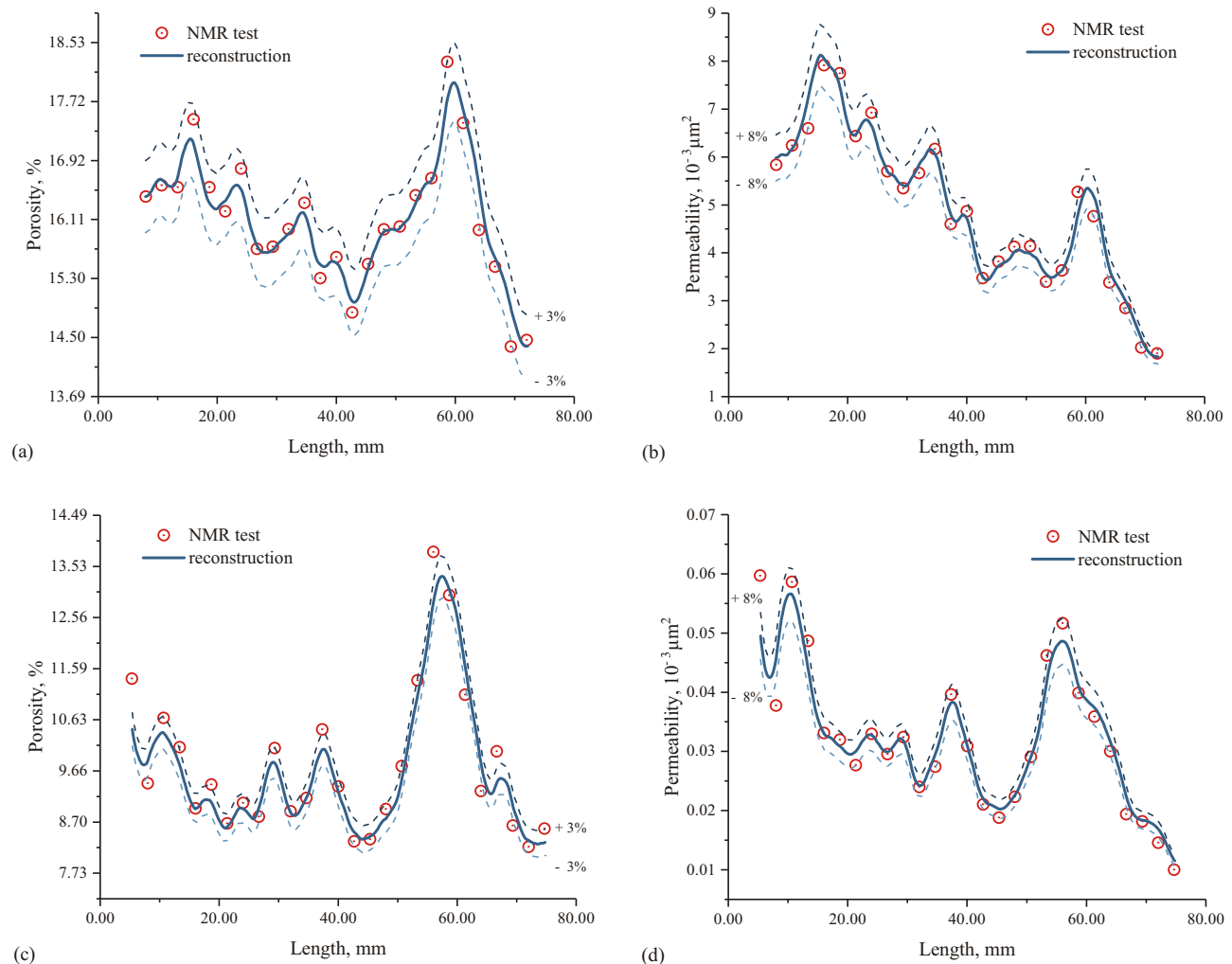


Figure 14: Porosity distribution of P58 samples (a) and Y75 samples (c) reconstruction model, and permeability distribution of P58 samples (b) and Y75 samples (d) reconstruction model.

parameters calculated by indirect method. Based on Eqs. (17) and (18), the local porosity distribution and permeability distribution of porous media can be obtained through the value conversion of  $A$  or  $T_{2A}$ , as shown in Figure 12, which is the local porosity distribution and permeability distribution map of P58 and Y75.

The color scale bar in the distribution map adopts the probability expression method, and the white scale is about 0.9971, 0.7207, 0.9381, and 1.050, which also approximately reflects that the local physical parameters are distributed around the physical parameters in the REV-scale, and a higher frequency occurs when the value is close to the macro value, and when the value is farther away from the macro value, lower frequency occurs.

## 4.2 Numerical verification

In order to verify the accuracy of the porous media model reconstructed by this method, REV-LBM [25] with multi-relaxation time is used to simulate the flow. In the simulation case, the kinematic viscosity is  $1.5 \times 10^{-7} \text{ m}^2/\text{s}$ , and the fluid density is  $1.1 \times 10^2 \text{ kg/m}^3$ . In addition, the fluid is driven by the fixed pressure gradient at both ends, which is always maintained at 0.0482 and 13.35 MPa/m in the case of P58 and Y75, respectively. The non-equilibrium extrapolation scheme is adopted for the inlet and outlet boundary, and the periodic boundary scheme is adopted for the upper and lower walls, as shown in Figure 13.

The standard homogeneous porous media model is to prove the accuracy of multi-relaxation time REV-LBM. The simulation result shows that the permeability calculation error is only 0.36% through the calculation formula  $K = \frac{\bar{u}\mu\Delta L}{\Delta P}$ , which indicates that the influence of the node number setting on the permeability calculation can be eliminated. The results of experimental measurement and reconstruction simulation are shown in Figure 14.

**Table 3:** Petrophysical parameters of the real samples and novel reconstruction models

	Y75 sample	Y75 model	P58 sample	P58 model
Porosity, %	9.66	9.66	16.11	16.11
Porosity error	—	0%	—	0%
Permeability, $10^{-3} \mu\text{m}^2$	0.03803	0.04092	4.655	4.941
Permeability error	—	7.60%	—	6.15%

**Table 4:** Petrophysical parameters of the real samples and digital rock [12]

	Real sample	CT-only digital rock	CT-SEM digital rock
Porosity, %	10.58	7.37	10.31
Porosity error	—	30.34%	2.55%
Permeability, $10^{-3} \mu\text{m}^2$	0.224	109	3.12
Permeability error	—	/	1,293%

Obviously, there is only an acceptable difference of 1D porous media parameters between the NMR tested and calculated based on the numerical simulation of the reconstructed model. For P58, the porosity and permeability error of almost all the measuring points can be maintained within 3–8%, respectively. While, for Y75, most measuring points have the errors within a certain range like P58, only a few measuring points at the end have a large error. Thus, this reconstruction model based on the previous generation method can describe the local characteristics of porous media well. Moreover, the overall permeability calculation error is about 6.15 and 7.60% based on the calculation formula  $K = \frac{\bar{u}\mu\Delta L}{\Delta P}$ , which also shows that the reconstructed porous medium model has good accuracy.

The calculation results of overall porosity and permeability of the reconstructed model are shown in Table 3. It can be found that the reconstructed model can always restore the measured porosity of the sample because the reconstructed model completely depends on the macro physical parameters of the actual sample. The permeability error of different samples can be controlled to be below 8%. Therefore, this porous media reconstruction method is suitable for porous media with different porosity and permeability. Compared with digital cores, the reconstruction error of the new model is far less than the existing 1,293% of digital core reconstruction error [12] (Table 4).

## 5 Conclusion

- 1) Based on spatially resolved  $T_2$  distribution measurement and combined with fractal statistical model, a new fine characterization modeling method for reconstructing porous media is proposed.
- 2) Through strict mathematical deduction, it is proved that the indirect method is more accurate in calculating

fractal parameters, and the method and proof of generating 2D fractal seed from two 1D fractal sequences are given.

- 3) REV-LBM is used to simulate the flow of the reconstructed fine porous media model. The simulation results show that the porous media model generated by this new method can reproduce the macro reservoir and seepage parameters of the original sample in a small error range, which is far less than the error of the existing digital core technology reconstruction model.
- 4) The new method of fine characterization and reconstruction modeling of porous media greatly shortens the experimental test cycle of the existing methods of porous media reconstruction (image analysis and digital core) and reduces the corresponding experimental cost. In addition, because this new method relies on nuclear magnetic testing technology, it is easy to operate and implement, and has broad prospects for development.

**Funding information:** This study is financially supported by Research on Comprehensive Evaluation Method of Unconventional Reservoir Based on Artificial Intelligence (2019D-500809), Study on the Seepage Law of Typical Low-Grade Oil Reservoirs and New Methods for Enhancing Oil Recovery (2021DJ1102), and Research on Tight Oil Physical Simulation and Production Mechanism (2021DJ2204).

**Author contributions:** All authors have accepted responsibility for the entire content of this manuscript and approved its submission.

**Conflict of interest:** The authors state no conflict of interest.

## References

- [1] Zhao X, Yang Z, Lin W, Xiong S, Wei Y. Characteristics of microscopic pore-throat structure of tight oil reservoirs in Sichuan basin measured by rate-controlled mercury injection. *Open Phys.* 2018;16(1):675–84.
- [2] Zhao X, Yang Z, Lin W, Xiong S, Luo Y, Wang Z, et al. Study on pore structures of tight sandstone reservoirs based on nitrogen adsorption, high-pressure mercury intrusion, and rate-controlled mercury intrusion. *J Energy Resour Technol.* 2019;141(11):112903.
- [3] Xiao Q, Yang Z, Wang Z, Qi Z, Wang X, Xiong S. A full-scale characterization method and application for pore-throat radius distribution in tight oil reservoirs. *J Pet Sci Eng.* 2020;187:106857.
- [4] Wang FY, Yang K, Zai Y. Multifractal characteristics of shale and tight sandstone pore structures with nitrogen adsorption and nuclear magnetic resonance. *Pet Sci.* 2020;17(5):1209–20.
- [5] Liu C, Yin C, Lu J, Sun L, Wang Y, Hu B, et al. Pore structure and physical properties of sandy conglomerate reservoirs in the Xujiaweizi depression, Northern Songliao Basin, China. *J Pet Sci Eng.* 2020;192:107217.
- [6] Qiao P, Ju Y, Cai J, Zhao J, Zhu H, Yu K, et al. Micro-nanopore structure and fractal characteristics of tight sandstone gas reservoirs in the Eastern Ordos Basin, China. *J Nanosci Nanotechnol.* 2021;21(1):234–45.
- [7] Wang Q, Chen D, Gao X, Wang F, Li J, Liao W, et al. Microscopic pore structures of tight sandstone reservoirs and their diagenetic controls: A case study of the upper triassic Xujiaweizi Formation of the Western Sichuan Depression, China. *Mar Pet Geol.* 2020;113:104119.
- [8] Cheng Z, Ning Z, Zhao H, Wang Q, Zeng Y, Wu X, et al. A comprehensive characterization of North China tight sandstone using Micro-CT, SEM imaging, and mercury intrusion. *Arab J Geosci.* 2019;12(13):1–8.
- [9] Lin W, Li X, Yang Z, Xiong S, Luo Y, Zhao X. Modeling of 3D rock porous media by combining X-Ray CT and Markov Chain Monte Carlo. *J Energy Resour Technol.* 2020;142(1):13001.
- [10] Lin W, Li X, Yang Z, Lin L, Xiong S, Wang Z, et al. A new improved threshold segmentation method for scanning images of reservoir rocks considering pore fractal characteristics. *Fractals.* 2018;26(2):1840003.
- [11] Lin W, Li X, Yang Z, Wang J, Xiong S, Luo Y, et al. Construction of dual pore 3-D digital cores with a hybrid method combined with physical experiment method and numerical reconstruction method. *Transp Porous Media.* 2017;120(1):227–38.
- [12] Lin W, Li X, Yang Z, Manga M, Fu X, Xiong S, et al. Multiscale digital porous rock reconstruction using template matching. *Water Resour Res.* 2019;55(8):6911–22.
- [13] Zhang T, Javadpour F, Yin Y, Li X. Upscaling water flow in composite nanoporous shale matrix using lattice Boltzmann method. *Water Resour Res.* 2020;56(4):e2019WR026007.
- [14] Liu Q, Feng XB. Lattice Boltzmann model for upscaling of flow in heterogeneous porous media based on Darcy's Law. *J Porous Media.* 2019;22(9):1131–9.
- [15] Sadeghnejad S, Enzmann F, Kersten M. Digital rock physics, chemistry, and biology: Challenges and prospects of pore-scale modelling approach. *Appl Geochem.* 2021;131:105028.
- [16] Monaretto T, Montrazi ET, Moraes TB, Souza AA, Rondeau-Mouro C, Colnago LA. Using T1 as a direct detection dimension in two-dimensional time-domain NMR experiments using CWFPP regime. *J Magnetic Reson.* 2020;311:106666.
- [17] Li L, Han H, Balcom BJ. Spin echo SPI methods for quantitative analysis of fluids in porous media. *J Magnetic Reson.* 2009;198(2):252–60.
- [18] Vashae S, Marica F, Newling B, Balcom BJ. A comparison of magnetic resonance methods for spatially resolved T<sub>2</sub> distribution measurements in porous media. *Meas Sci & Technol.* 2015;26(5):055601.

- [19] Wang L, Mao ZQ, Sun ZC, Luo XP, Deng RS, Zhang YH, Ren B. Cation exchange capacity ( $Q_v$ ) estimation in shaly sand reservoirs: Case studies in the Junggar Basin, Northwest China. *J Geophys Eng.* 2015;12(5):745–52.
- [20] Rezaee R, Saeedi A, Clennell B. Tight gas sands permeability estimation from mercury injection capillary pressure and nuclear magnetic resonance data. *J Pet Sci Eng.* 2012;88–89:92–9.
- [21] Lyu C, Ning Z, Cole DR, Wang Q, Chen M. Experimental investigation on  $T_2$  cutoffs of tight sandstones: Comparisons between outcrop and reservoir cores. *J Pet Sci Eng.* 2020;191:107184.
- [22] Mandelbrot BB, Van Ness JW. Fractional Brownian motions, fractional noises and applications. *SIAM Rev.* 1968;10(4):422–37.
- [23] Koch S, Neuenkirch A. The Mandelbrot-van Ness fractional Brownian motion is Infinitely Differentiable with Respect to Its Hurst Parameter. *Discret Contin Dyn Syst - B.* 2019;24(8):3865–80.
- [24] Lau W, Erramilli A, Wang JL, Willinger W. Self-Similar Traffic Generation: the Random Midpoint Displacement Algorithm and Its Properties [C]. *Proceedings IEEE International Conference on Communications ICC '95*; 1995.
- [25] Guo ZL, Zhao TS. Lattice Boltzmann model for incompressible flows through porous media. *Phys Rev E.* 2002;66(3):36304.



## Appendix

### Appendix I

Define  $f(x) = B(x + \Delta x) - B(x)$ ,  $f(y) = B(y + \Delta y) - B(y)$ .

Because of  $B_{2D}(x, y) = \frac{|B(x)\rangle\langle B(y)|}{\mu_B}$ , by analogy with the definition of 1D, we can get,

X-axis direction:

$$\begin{aligned} f_{x-2D}(x, y) &= B_{2D}(x + \Delta x, y) - B_{2D}(x, y) \\ &= \frac{1}{\mu_B}(|B(x + \Delta x)\rangle\langle B(y)| - |B(x)\rangle\langle B(y)|). \end{aligned}$$

Y-axis direction:

$$\begin{aligned} f_{y-2D}(x, y) &= B_{2D}(x, y + \Delta y) - B_{2D}(x, y) \\ &= \frac{1}{\mu_B}(|B(x)\rangle\langle B(y + \Delta y)| - |B(x)\rangle\langle B(y)|). \end{aligned}$$

After sorting out, they are  $f_{x-2D}(x, y) = \frac{1}{\mu_B}|f(x)\rangle\langle B(y)|$  and  $f_{y-2D}(x, y) = \frac{1}{\mu_B}|B(x)\rangle\langle f(y)|$ , respectively. It is obvious that  $f_{x-2D}(x, y)$  and  $f(x)$  have the same fractal properties, while  $f_{y-2D}(x, y)$  and  $f(y)$  have the same fractal properties.

### Appendix II

For the direct method, in the X direction,  $D[f_{x-2D}(x, y)] = E[f_{x-2D}^2(x, y)] - E^2[f_{x-2D}(x, y)]$ , the two parts on the right side of the equation can be expanded as,

$$\begin{aligned} E[f_{x-2D}^2(x, y)] &= E\left\{\left[\frac{1}{\mu_B}|f(x)\rangle\langle B(y)|\right]^2\right\} \\ &= \frac{1}{\mu_B^2}E\{|f(x)\rangle\langle B(y)|\}^2 \\ &= \frac{E[B^2(y)]}{\mu_B^2}E[f^2(x)], \end{aligned}$$

$$\begin{aligned} E^2[f_{x-2D}(x, y)] &= E^2\left[\frac{1}{\mu_B}|f(x)\rangle\langle B(y)|\right] \\ &= \left\{\frac{1}{\mu_B}E[f(x)]E[B(y)]\right\}^2 \\ &= E^2[f(x)]. \end{aligned}$$

After sorting out

$$D[f_{x-2D}(x, y)] = \frac{E[B^2(y)]}{\mu_B^2}E[f^2(x)] - E^2[f(x)]. \quad (A1)$$

In the same way, we can get the value in the Y direction

$$D[f_{y-2D}(x, y)] = \frac{E[B^2(x)]}{\mu_B^2}E[f^2(y)] - E^2[f(y)]. \quad (A2)$$

For 1D fractal scatter sequence

$$D[f(x)] = E[f^2(x)] - E^2[f(x)], \quad (A3)$$

$$D[f(y)] = E[f^2(y)] - E^2[f(y)]. \quad (A4)$$

It can be found that for finite scatters

$E[f(x)] \neq 0$  and  $E[f(y)] \neq 0$ , at this time  $\frac{D[f_{x-2D}(x, y)]}{D[f(x)]}$

and  $\frac{D[f_{y-2D}(x, y)]}{D[f(y)]}$  are not constant values. The change in dimension will cause the change in Hurst exponent. But ingeniously, when the sample size of the observation data is large enough,  $E[f(x)] \rightarrow 0$ ,  $E[B^2(y)] \approx \sigma_{By}^2 + \mu_B^2$  and  $E[f(y)] \rightarrow 0$ ,  $E[B^2(x)] \approx \sigma_{Bx}^2 + \mu_B^2$ , Eqs. (A1) and (A2) can be written separately.

$$D[f_{x-2D}(x, y)] = (1 + cv_y^2)D[f(x)], \quad (A5)$$

$$D[f_{y-2D}(x, y)] = (1 + cv_x^2)D[f(y)]. \quad (A6)$$

In this case, the Hurst exponent calculated by the direct method also does not change with the change in dimension, and it is uniformly invariant.

For the indirect method, in the X direction

$$\begin{aligned} E[|f_{x-2D}(x, y)|] &= E\left[\left|\frac{1}{\mu_B}|f(x)\rangle\langle B(y)|\right|\right] \\ &= \frac{1}{\mu_B}E[|f(x)\rangle\langle B(y)|] \\ &= E[|f(x)|]. \end{aligned} \quad (A7)$$

Similarly, along the Y direction

$$E[|f_{y-2D}(x, y)|] = E[|f(y)|]. \quad (A8)$$

Obviously,  $\frac{E[|f_{x-2D}(x, y)|]}{E[|f(x)|]} = \frac{E[|f_{y-2D}(x, y)|]}{E[|f(y)|]} = 1$ . At this time, the calculated Hurst exponent and the standard deviation  $\sigma_0$  under reference distance  $\Delta_0$  will not change with the change in dimension.